

Superconducting Gap Function in an Organic Superconductor (TMTSF)₂ClO₄ with Anion Ordering; First-principles Calculations and Quasi-classical Analyses for Angle-resolved Heat Capacity

Yuki Nagai,^{1,2} Hiroki Nakamura,^{1,2} and Masahiko Machida^{1,2}

¹CCSE, Japan Atomic Energy Agency, 6-9-3 Higashi-Ueno, Tokyo 110-0015, Japan

²CREST(JST), 4-1-8 Honcho, Kawaguchi, Saitama, 332-0012, Japan

(Dated: November 11, 2018)

We calculate angle-dependent heat capacity in a low magnetic field range on the basis of Kramer-Pesch approximation together with an electronic structure obtained by first-principles calculations to determine a superconducting gap function of (TMTSF)₂ClO₄ through its comparisons with experiments. The present comparative studies reveal that a nodal *d*-wave gap function consistently explains the experimental results for (TMTSF)₂ClO₄. Especially, it is emphasized that the observed unusual axis-asymmetry of the angle-dependence eliminates the possibility of *s*-wave and node-less *d*-wave functions. It is also found that the directional ordering of ClO₄ anions does not have any significant effects on the Fermi surface structure contrary to the previous modelings since the two Fermi surfaces obtained by the band calculations almost cross within the present full accuracy in first-principles calculations.

PACS numbers: 71.15.Mb, 74.25.Jb, 74.20.Rp, 74.25.Bt

I. INTRODUCTION

The organic superconductors, (TMTSF)₂X's have attracted considerable attention because of their rich variety of phases including superconducting states in spite of rather simple quasi-one-dimensional (Q1D) electronic structures. For example, (TMTSF)₂PF₆ exhibits a pressure induced superconductivity whose pairing symmetry has been expected to be spin-triplet by Knight-shift measurements¹. Meanwhile, (TMTSF)₂ClO₄ is an ambient pressure superconductor, whose Knight-shift measurements suggest a conventional spin-singlet pairing². Since the singlet superconducting phase is in close proximity to spin density wave (SDW) states, spin-fluctuation has been proposed as a candidate of the pairing glue. However, the pairing mechanism is still far from an established settlement for (TMTSF)₂X in spite of several theoretical studies³⁻⁹.

Synchronous to the theoretical struggle, a number of experimental studies have been also made to clarify the superconducting pairing symmetry for (TMTSF)₂ClO₄. The superconducting transition temperature for (TMTSF)₂(ClO₄)_{1-x}(ReO₄)_x is suppressed by a tiny amount of non-magnetic impurities.¹⁰ Such a result may be evidence of the presence of nodes in the superconducting gap function. Moreover, Takigawa *et al.* found that the nuclear magnetic relaxation rate lacks a coherence peak below T_c together with a low temperature power-law behavior ($1/T_1 \sim T^3$)¹¹. These results suggest that the gap function has line-nodes at which the sign of the gap function changes. On the other hand, Belin and Behnia showed that the thermal conductivity rapidly decreases below T_c . The data leads to the absence of any nodal structures¹².

Recently, a technique rotating the applied magnetic field has been incorporated in thermal measurements

such as heat capacity and thermal conductivity measurements to probe the gap structure including positions of gap nodes in more details^{13,14}. The angle-resolved heat capacity measurement is one of such advanced measurements, in which one detects details of the gap structure, especially locations of its nodes by measuring the oscillation of the heat capacity $C(\mathbf{H})$ with respect to the applied magnetic field \mathbf{H} direction. The rotational dependence on the thermal conductivity is also a powerful tool to examine gap structures similarly. In this paper, we propose Kramer-Pesch approximation (KPA) together with first-principles electronic-structure calculations as a new theoretical tool to analyze the advanced angle-dependent-measurement data¹⁵. KPA significantly exceeds the accuracy level of the previous Doppler shift approximation. We have calculated the density of states (DOS's) around a vortex by using anisotropic Fermi surfaces¹⁵⁻¹⁷ obtained by first-principles calculations and compare calculated angle dependences of heat capacity with the experimental data.

Very recently, Yonezawa *et al.* reported that the oscillation curve of the heat capacity $C(\mathbf{H})/T$ for (TMTSF)₂ClO₄ obtained by rotating the field becomes asymmetric with respect to the crystalline *a*-axis in the low temperature and low field range.¹⁸ In addition, kink structures are observed near this *a*-axis direction. They claimed, based on the Doppler shift analysis, that the asymmetries and the kink structures are clear evidence for the presence of line-nodes.

On the other hand, a structural phase transition corresponding to an anion ordering was observed at 24 K for (TMTSF)₂ClO₄¹⁹⁻²¹. Shimahara proposed a nodeless fully-gapped *d*-wave superconductivity associated with the anion order⁸. Afterwards, several theoretical studies have suggested effective models with or without the anion ordering to discuss the pairing mechanism.^{3-7,9} However,

there has been no first-principles calculation taking account of the anion ordering. Here, we emphasize that a trustful band calculation resolves effects of the anion ordering on the electronic structure.

The present paper has two objectives. The first one is to analyze the angle-resolved heat capacity for (TMTSF)₂ClO₄ with Fermi surfaces obtained by first-principles calculations. We identify the superconducting gap function by using an expression for the heat capacity on the basis of KPA in a low temperature and low magnetic field range. The KPA-based expression is applicable to various other unconventional superconductors. We calculate the heat capacity by assuming the *s*-wave, nodeless *d*-wave and nodal *d*-wave gap functions and compare the results with the measurement data. The second one is to examine the effects of the anion ordering on the electronic structure of (TMTSF)₂ClO₄. We clarify the electronic structure, especially Fermi surfaces through first-principles calculations using the measured structure parameters in the anion-ordered state.

The rest of this paper is organized as follows. The quasiclassical approximation to describe the superconducting state is briefly introduced in Sec. II. Then, the KPA calculation scheme based on the quasiclassical approach is presented in Sec. III. We derive a vortex solution using KPA and present an expression of the heat capacity around a vortex. The electronic structure of (TMTSF)₂ClO₄ by first-principles calculations is given in Sec. IV, in which we display the band structure and Fermi surfaces. The calculation results on the angle-dependent heat capacity are shown in Sec. V. The discussion and conclusion are, respectively, given in Sec. VI. and VII.

II. QUASICLASSICAL THEORY OF SUPERCONDUCTIVITY

In many BCS superconductors, the gap-amplitude is much smaller than the Fermi energy, $|\Delta| \ll E_F$. In this case, one can properly use a quasiclassical approximation²²⁻²⁴. We consider the quasiclassical Green's function \check{g} that has the matrix elements in the Nambu (particle-hole) space as

$$\check{g}(z, \mathbf{r}, \mathbf{k}_F) \equiv \begin{pmatrix} g & f \\ -\tilde{f} & -g \end{pmatrix}, \quad (1)$$

which is a 2×2 matrix in the Nambu space and is a function of complex frequency z , Fermi wave-vector \mathbf{k}_F , and point \mathbf{r} in real space. We set $\hbar = k_B = 1$ through this paper. The equation of motion for \check{g} is written as

$$-i\mathbf{v}_F(\mathbf{k}_F) \cdot \nabla \check{g} = [z\check{\tau}_3 - \check{\Delta}(\mathbf{r}, \mathbf{k}_F), \check{g}], \quad (2)$$

with Fermi velocity \mathbf{k}_F and the commutator $[\check{a}, \check{b}] = \check{a}\check{b} - \check{b}\check{a}$ supplemented by the normalization condition

$$\check{g}^2 = -\pi^2 \check{1}. \quad (3)$$

Here, $\check{\Delta}$ is given by

$$\check{\Delta}(\mathbf{r}, \mathbf{k}_F) = \begin{pmatrix} 0 & \Delta(\mathbf{r}, \mathbf{k}_F) \\ -\Delta^*(\mathbf{r}, \mathbf{k}_F) & 0 \end{pmatrix}. \quad (4)$$

We neglect the vector potential by confining ourselves in type II limit. Setting $z = \epsilon + i\eta$ with infinitesimal positive η , we obtain the retarded quasiclassical Green's function \check{g}^R . In this paper, we use a special parameterization of the quasiclassical Green's function to solve Eq. (2).²⁵⁻³⁰ The solution \check{g} of Eq. (2) can be written as

$$\check{g} = \frac{-i\pi}{1+ab} \begin{pmatrix} 1-ab & 2ia \\ -2ib & -(1-ab) \end{pmatrix}, \quad (5)$$

where a and b are the solutions of the following Riccati differential equations:

$$\mathbf{v}_F(\mathbf{k}_F) \cdot \nabla a = 2iza - a^2\Delta^* + \Delta, \quad (6)$$

$$\mathbf{v}_F(\mathbf{k}_F) \cdot \nabla b = -2izb + b^2\Delta - \Delta^*. \quad (7)$$

In the parameterization Eq. (5), the normalization condition Eq. (3) is automatically satisfied.³²

Since Eqs. (6) and (7) contain ∇ only through $\mathbf{v}_F(\mathbf{k}_F) \cdot \nabla$, they are reduced to a one-dimensional problem on a straight line, the direction of which is given by that of the Fermi velocity $\mathbf{v}_F(\mathbf{k}_F)$. We consider a single vortex along the z_M axis. Because of the translational symmetry along the z_M axis, the pair potential Δ does not depend on z_M in the Riccati equations (6) and (7), and hence the Riccati equations can be rewritten as

$$v_{F\perp}(\mathbf{k}_F) \frac{\partial}{\partial s} a = 2iza - a^2\Delta^*(s, y, \mathbf{k}_F) + \Delta(s, y, \mathbf{k}_F), \quad (8)$$

$$v_{F\perp}(\mathbf{k}_F) \frac{\partial}{\partial s} b = -2izb + b^2\Delta(s, y, \mathbf{k}_F) - \Delta^*(s, y, \mathbf{k}_F), \quad (9)$$

where $v_{F\perp}(\mathbf{k}_F)$ is the amplitude of the vector $v_{F\perp}(\mathbf{k}_F)$ perpendicular to the z_M axis by projecting the Fermi velocity $\mathbf{v}(\mathbf{k}_F)$ and the coordinate s (y) is along the direction parallel (perpendicular) to $\mathbf{v}_{F\perp}(\mathbf{k}_F)$. For simplicity, we solve the Riccati differential equations under a given form of the pair function. The density of states is given by

$$N(\epsilon) = \langle \nu(\mathbf{r}, \epsilon) \rangle_{SP}, \quad (10)$$

$$\nu(\mathbf{r}, \epsilon) = -\frac{1}{\pi} \int \frac{dS_F}{2\pi^2 |\mathbf{v}_F|} \text{Im} (g^R). \quad (11)$$

Here, $\langle \dots \rangle_{SP} \equiv \int_0^{r_a} r dr \int_0^{2\pi} d\alpha / (\pi r_a^2)$ is the real-space average around a vortex where $r_a/\xi_0 = \sqrt{H_{c2}/H}$ [$H_{c2} \equiv \Phi_0/(\pi\xi_0^2)$, $\Phi_0 = \pi r_a^2 H$] and dS_F is the Fermi-surface area element. By using $N(\epsilon)$, the low-temperature specific heat is given as

$$\frac{C(T)}{T} = \int_{-\infty}^{\infty} \frac{d\epsilon}{T} \frac{\epsilon^2}{T^2} \frac{N(\epsilon)}{\cosh^2(\frac{\epsilon}{2T})}. \quad (12)$$

III. KRAMER-PESCH APPROXIMATION

We introduce Kramer-Pesch approximation (KPA) as an efficient method to analyze the angle-resolved experiments. We have shown that KPA gives the zero-energy density of states around a vortex consistent quantitatively with results of direct numerical calculations¹⁵. In addition, the computational time required for KPA is almost the same as that for the Doppler Shift method, which is significantly less than that in direct numerical calculations. Furthermore, it is emphasized that KPA can calculate the density of states even in complicated Fermi surfaces without any heavy numerical computations. So far, we have actually examined various unconventional superconductors with the use of KPA^{15-17,31,32}.

In works based on KPA, there has been a different way in theoretical treatments on the vortex core. Mel'nikov *et al.* presented an analytical solution describing the anomalous branches in a single vortex with arbitrary winding numbers by generalizing the Caroli-de Gennes-Matricon approach³³. They also demonstrated that the analytical solution on a single vortex is valid even in a higher energy range near the gap-amplitude. Therefore, we incorporate the Mel'nikov's method to calculate the heat capacity. The Mel'nikov's method can be regarded as a perturbation with respect to both energy and imaginary part of the pair-function in the Riccati formalism.

Now, let us show the present scheme. First, we briefly mention the Doppler Shift method in the Riccati formalism for comparison. We separate the pair-potential Δ into the amplitude and the phase $\Phi(s, y, \mathbf{k}_F)$ as

$$\Delta(s, y, \mathbf{k}_F) = |\Delta(s, y, \mathbf{k}_F)| e^{i\Phi(s, y, \mathbf{k}_F)}. \quad (13)$$

Introducing $a = \exp(i\Phi)\tilde{a}$ and $b = \exp(-i\Phi)\tilde{b}$, the Riccati equation is written as

$$v_{F\perp}(\mathbf{k}_F) \frac{\partial}{\partial s} \tilde{a} = i \left(2z - v_{F\perp}(\mathbf{k}_F) \frac{\partial}{\partial s} \Phi \right) \tilde{a} - \tilde{a}^2 |\Delta| + |\Delta|, \quad (14)$$

$$v_{F\perp}(\mathbf{k}_F) \frac{\partial}{\partial s} \tilde{b} = -i \left(2z - v_{F\perp}(\mathbf{k}_F) \frac{\partial}{\partial s} \Phi \right) \tilde{b} + \tilde{b}^2 |\Delta| - |\Delta|. \quad (15)$$

Assuming $\partial\tilde{a}/\partial s = \partial\tilde{b}/\partial s = 0$, the equations can be exactly solved in an analytical way. The solution is equivalent to that in the bulk region by replacing the energy z with the Doppler shifted energy $z - (v_{F\perp}/2)(\partial\Phi/\partial s)$. The Doppler Shift method is an approximation neglecting the spatial variation of $|\tilde{a}| = |a|$. Then, it breaks down near a vortex core^{15,34}.

Next, we derive the vortex solution by using KPA. We write down a pair-potential around a vortex in the following form,

$$\Delta(s, y, \mathbf{k}_F) = f(s, y) \Delta_\infty d(\mathbf{k}_F) e^{i\theta_r}, \quad (16)$$

$$= f(s, y) \Delta_\infty d(\mathbf{k}_F) \frac{s + iy}{\sqrt{s^2 + y^2}} e^{i\theta_v(\mathbf{k}_F)}, \quad (17)$$

where $f(s, y)$ describes the spatial variation of the pair-potential. Then, $f(0) = 0$, $\lim_{r \rightarrow \infty} f(r) = 1$, and Δ_∞ is a pair-potential in the bulk region. θ_r denotes an angle around a vortex and θ_v does a direction of the projected Fermi velocity $\mathbf{v}_{F\perp}(\mathbf{k}_F)$ ³². Introducing the variables written as

$$a = \bar{a} e^{i\theta_v}, \quad (18)$$

$$b = \bar{b} e^{-i\theta_v}, \quad (19)$$

$$\Delta = \bar{\Delta} e^{i\theta_v}, \quad (20)$$

the Riccati equations are rewritten as

$$v_{F\perp}(\mathbf{k}_F) \frac{\partial}{\partial s} \bar{a} = 2iz\bar{a} - \bar{a}^2 \bar{\Delta}^* + \bar{\Delta}, \quad (21)$$

$$v_{F\perp}(\mathbf{k}_F) \frac{\partial}{\partial s} \bar{b} = -2iz\bar{b} + \bar{b}^2 \bar{\Delta} - \bar{\Delta}^*. \quad (22)$$

In KPA with the Riccati formalism as the previous paper^{15-17,31,32}, we expand \bar{a} and \bar{b} in Eqs. (21) and (22) with respect to the impact parameter y and the complex frequency z . In this paper, we expand these variables with respect to the imaginary part of the pair-function $\bar{\Delta}$, in stead of y , and the complex frequency z on the basis of the Mel'nikov's method. Then, Δ_R and Δ_I are defined as

$$\Delta_R = \text{Re } \bar{\Delta} = f(s, y) \Delta_\infty d(\mathbf{k}_F) \frac{s}{\sqrt{s^2 + y^2}}, \quad (23)$$

$$\Delta_I = \text{Im } \bar{\Delta} = f(s, y) \Delta_\infty d(\mathbf{k}_F) \frac{y}{\sqrt{s^2 + y^2}}. \quad (24)$$

Following Refs. 25 and 32, we eventually obtain \bar{a} and \bar{b} as

$$\bar{a} = \bar{a}_0 + \bar{a}_1 + \mathcal{O}(z^2, \Delta_I^2, z\Delta_I), \quad (25)$$

$$\bar{b} = \bar{b}_0 + \bar{b}_1 + \mathcal{O}(z^2, \Delta_I^2, z\Delta_I), \quad (26)$$

with

$$\bar{a}_0 = -\text{sign}(d(\mathbf{k}_F)), \quad (27)$$

$$\bar{b}_0 = \text{sign}(d(\mathbf{k}_F)), \quad (28)$$

$$\bar{a}_1(s) = \frac{e^{u(s)}}{v_{F\perp}(\mathbf{k}_F)} \int_{-\infty}^s (2i\bar{a}_0 z + 2i\Delta_I(s')) e^{-u(s')} ds' \quad (29)$$

$$\bar{b}_1(s) = \frac{e^{u(s)}}{v_{F\perp}(\mathbf{k}_F)} \int_{\infty}^s (-2i\bar{b}_0 z + 2i\Delta_I(s')) e^{-u(s')} ds'. \quad (30)$$

Together with the help of the following function,

$$u(s) = 2 \frac{|d(\mathbf{k}_F)|}{v_{F\perp}(\mathbf{k}_F)} \int_0^s \Delta_\infty f(s', y) \frac{s'}{\sqrt{s'^2 + y^2}} ds', \quad (31)$$

the quasiclassical Green's function is then written as

$$\check{g} \sim \frac{-2\pi i}{\bar{a}_1 \bar{b}_0 + \bar{a}_0 \bar{b}_1} \check{M}, \quad (32)$$

$$= \frac{\pi v_{F\perp}(\mathbf{k}_F)}{C(y, \mathbf{k}_F)} \frac{e^{-u(s)}}{z - E(y, \mathbf{k}_F)} \check{M}, \quad (33)$$

with

$$\tilde{M} \equiv \begin{pmatrix} 1 & ia_0 \\ -ib_0 & -1 \end{pmatrix}, \quad (34)$$

$$C(y, \mathbf{k}_F) \equiv \int_{-\infty}^{\infty} e^{-u(s')} ds', \quad (35)$$

$$E(y, \mathbf{k}_F) \equiv \frac{|d(\mathbf{k}_F)|\Delta_\infty}{C(y, \mathbf{k}_F)} \int_{-\infty}^{\infty} f(s', y) \frac{y}{\sqrt{s'^2 + y^2}} e^{-u(s')} ds'. \quad (36)$$

The quasiclassical Green's function has the pole at $z = E(y, \mathbf{k}_F)$, which is regarded as energy of quasi-particle. Substituting Eq. (33) into Eqs. (11) and (12) and setting $z = \epsilon + i\eta$, the density of states is given as

$$N(\epsilon) = \left\langle \int \frac{dS_F}{2\pi^2 |\mathbf{v}_F|} \frac{v_{F\perp}(\mathbf{k}_F)}{C(y, \mathbf{k}_F)} e^{-u(s)} \delta(\epsilon - E(y, \mathbf{k}_F)) \right\rangle_{\text{SP}}. \quad (37)$$

Thus, we obtain the heat capacity in the clean-limit ($\eta \rightarrow 0$) with the use of the KPA written as

$$\frac{C(T)}{T} = \left\langle \int \frac{dS_F v_{F\perp}(\mathbf{k}_F)}{2\pi^2 |\mathbf{v}_F| T^3} \frac{E(y, \mathbf{k}_F)^2}{C(y, \mathbf{k}_F)} \frac{e^{-u(s)}}{\cosh^2\left(\frac{E(y, \mathbf{k}_F)}{2T}\right)} \right\rangle_{\text{SP}}. \quad (38)$$

On the other hand, we set the spatial variation of the pair-potential $f(s, y)$ as

$$f(s, y) = \frac{r}{\sqrt{r^2 + \xi_0^2}} = \frac{\sqrt{s^2 + y^2}}{\sqrt{s^2 + y^2 + \xi_0^2}}. \quad (39)$$

With the use of this function, one can integrate Eqs. (35) and (36):

$$C(y, \mathbf{k}_F) = 2\sqrt{y^2 + \xi_0^2} K_1(r_0(y, \mathbf{k}_F)), \quad (40)$$

$$E(y, \mathbf{k}_F) = |d(\mathbf{k}_F)|\Delta_\infty \frac{y}{\sqrt{y^2 + \xi_0^2}} \frac{K_0(r_0(y, \mathbf{k}_F))}{K_1(r_0(y, \mathbf{k}_F))}, \quad (41)$$

with

$$r_0(y, \mathbf{k}_F) \equiv \frac{2|d(\mathbf{k}_F)|\Delta_\infty}{v_{F\perp}(\mathbf{k}_F)} \sqrt{y^2 + \xi_0^2}. \quad (42)$$

where, the function $K_n(x)$ is the modified Bessel function of the second kind.

IV. BAND STRUCTURE

Now, let us display the electronic structure. In order to calculate the band structure, we employ a first-principles density-functional-calculation package VASP³⁵. Among available options for the band calculations, we adopt GGA exchange-correlation energy³⁶ and PAW method³⁷ due to their excellent computational performance as well

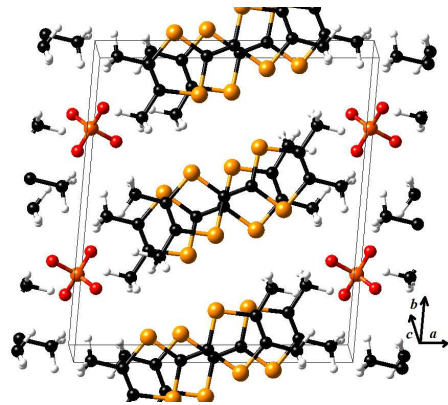


FIG. 1. (Color online) Crystal structure for $(\text{TMTSF})_2\text{ClO}_4$.

as accuracy. The lattice constants and atomic inner-coordinates refer to a measurement report, Ref. 38. The calculation self-consistent loops to obtain a converged electronic structure are repeated until the total energy difference becomes smaller than 10^{-6} eV. In the loops, k -points are taken as $10 \times 5 \times 5$, and the energy cut-off is set to be 500 eV. Once the electron density is obtained after the convergence, the energy bands are again calculated on finer k -points as $49 \times 23 \times 25$ in order to determine the Fermi surfaces and the Fermi velocities accurately as much as possible.

Since the employed structural parameters are measured at 7K, the data reflects the orientational ordering of the tetrahedral ClO_4 anions in the crystal structure of $(\text{TMTSF})_4\text{ClO}_4$. The ordered structure is displayed in Fig. 1. We obtain the band structure and Fermi surface for the structural parameters as shown in Fig. 2 and 3. From Fig. 3, it is found that the two Fermi surfaces almost cross each other since the anion ordering gap is too small to resolve it in the standard scale. The tiny gap can be distinguished only by an enlarged scope as the inset of Fig.3. This result clearly suggests that the direction of the ClO_4 anion ordering does not have any significant effect on the Fermi surface structure contrary to the previous theoretical expectations. Thus, we would like to point out that any theoretical modelings originated from the anion ordering are unlikely to consistently explain recent advanced experimental data.

V. RESULTS

We study the angle-resolved heat capacity, in which the applied magnetic field is rotated inside the basal a - b -plane. Three pairing symmetries are employed to test their matching with the angle-resolved experimental results. For simplicity, we assume that the vortex core is cylindrically isotropic and anisotropy of the critical magnetic field is not present, i.e., $H_{c2}(\phi) \sim H_{c2}$. On the analysis of the vortex core excitation, we set a spatial cutoff length $r_a = 5\xi_0$, which is comparable to the neighboring

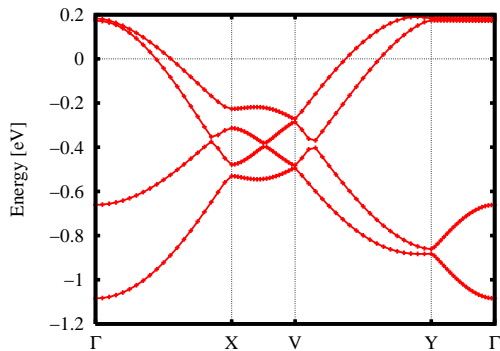


FIG. 2. (Color online) Band structure for $(\text{TMTSF})_2\text{ClO}_4$.

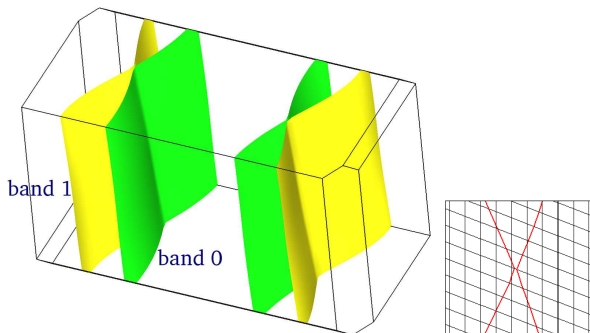


FIG. 3. (Color online) Fermi surfaces for $(\text{TMTSF})_2\text{ClO}_4$. Inset: Closeup of the Fermi-surface crossing, sliced at $k_z = 0$. The mesh describes k -points actually used in the Fermi-surface calculation.

vortex distance as the magnetic field $H \sim H_{c2}/25$. We take the x -axis (y -axis) parallel (perpendicular) to the a -axis. It is also noted that y -axis is parallel to the b' -axis introduced by the Ref. 39 on a - b -plane and z -axis is perpendicular to the a - b -plane.

A. s -wave gap function

First, we examine a possibility of an isotropic s -wave gap function. In this case, the oscillation pattern of the angle resolved heat capacity suffers only the Fermi surface anisotropy. As shown in Fig. 4, the heat capacity curve monotonically oscillates with the angle ϕ and shows the minima at $\phi = 0$ reflecting the Fermi surface anisotropy. The minima appear as the magnetic field direction is parallel to the a -axis. This oscillatory pattern is as one expects, but inconsistent with the latest measurement data in details. In terms of the minima, we note that the Doppler shift method can not resolve even these minima, since the Doppler shift method can not describe the Fermi surface anisotropy in fully-gapped superconductors. Meanwhile, in the present scheme using KPA, the momentum \mathbf{k}_F dependent kernel of the heat capacity (the integrand in Eq. (38)) vanishes as the magnetic field

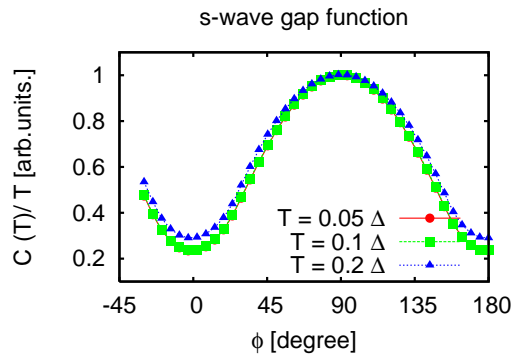


FIG. 4. (Color online) Angular dependence of the heat capacity rotating magnetic fields on a - b' plane in the case of the s -wave gap function.

is directed parallel to the Fermi velocity $v(\mathbf{k}_F)$, since the projected Fermi velocity $v_{F\perp}(\mathbf{k}_F)$ then becomes zero. In the case of $(\text{TMTSF})_2\text{ClO}_4$, the Fermi velocity is almost parallel to the a -axis on the whole Fermi surfaces because of the quasi-one-dimensionality.

B. Nodeless d -wave gap function

Next, we check a possibility of the nodeless d -wave gap function proposed by Shimahara.⁸ We employ the nodeless d -wave gap function expressed as (see Fig. 5)

$$\Delta^0(k_x, k_y, k_z) = a_0 f^0(k_x, k_y + b_0), \quad (43)$$

$$\Delta^1(k_x, k_y, k_z) = -(a_1 f^1(k_x, k_y) + b_1), \quad (44)$$

with

$$f^0(k_x, k_y) \equiv \cos\left(\left(k_y - k_0\right)\frac{2\pi}{g_y}\right) - \frac{1}{2} \cos\left(2\left(k_y - k_0\right)\frac{2\pi}{g_y}\right), \quad (45)$$

$$f^1(k_x, k_y) \equiv \cos\left(\left(k_y - k_0\right)\frac{2\pi}{g_y}\right), \quad (46)$$

$$k_0 \equiv -0.031 \text{ sign}(k_x). \quad (47)$$

where, $a_{0,1}$ and $b_{0,1}$ denote normalization factors ($a_0 = 10/26$, $b_0 = -17/26$, $a_1 = 10/23$ and $b_1 = -3/23$), g_y is the second element of the reciprocal lattice vector defined by $g_y = 2\pi/(b \sin \gamma)$, b denotes the crystal axis $b = 15.356 \text{ \AA}$, $\gamma = 68.92^\circ$, and k_0 denotes the intersection of two Fermi surfaces. As shown in Fig. 6, a slightly concave but almost flat-like curve showing the minimum at the center lies around the angles $-20^\circ < \phi < 20^\circ$. These symmetric kink-like curvature including the unclear minimum is due to anisotropy of the Fermi surface and the gap function. Close to $k_y = k_0$, the Fermi velocity continuously changes its direction around the a -axis, and the amplitude of the gap function gives the minimum with no change of the gap sign as shown in Fig. 5. Therefore, the angle variation of the magnetic field around a -axis

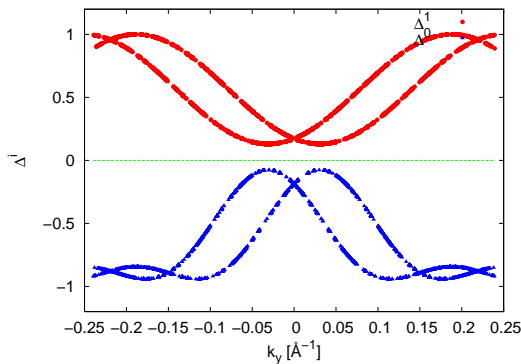


FIG. 5. (Color online) Gap functions on the Fermi surfaces in the case of the nodeless d -wave gap function.

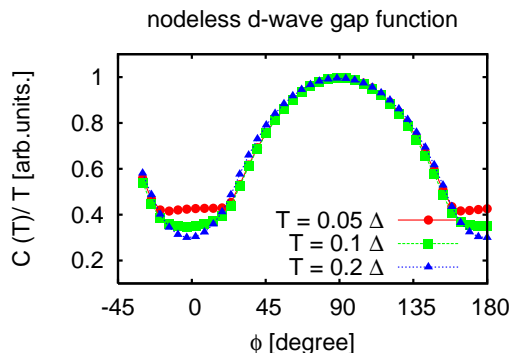


FIG. 6. (Color online) Angular dependence of the heat capacity rotating magnetic fields on a - b' plane in the case of the nodeless d -wave gap function.

($-20^\circ < \phi < 20^\circ$) is almost lost, i.e., DOS's of the quasi-particles with the small gap do not almost change with the angle. These results are inconsistent with the measurement data.

C. Nodal d -wave gap function

Finally, we examine nodal d -wave gap functions. The trial nodal d -wave gap functions are classified into three types expressed as

$$\Delta^0(k_x, k_y, k_z) = \begin{cases} f(k_x, k_y) & (\text{case I}) \\ f(k_x, k_y) & (\text{case II}) \\ 1 & (\text{case III}) \end{cases}, \quad (48)$$

$$\Delta^1(k_x, k_y, k_z) = \begin{cases} f(k_x, k_y) & (\text{case I}) \\ 1 & (\text{case II}) \\ f(k_x, k_y) & (\text{case III}) \end{cases}, \quad (49)$$

with

$$f(k_x, k_y) \equiv \cos\left(k_y \frac{2\pi}{b_y}\right). \quad (50)$$

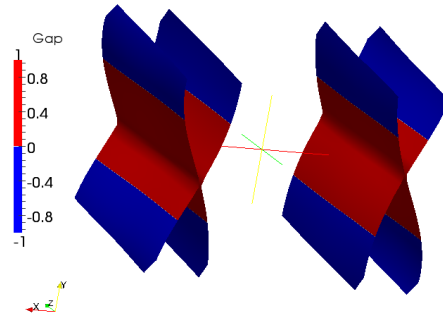


FIG. 7. (Color online) Schematic figure about the nodal line in the case of the nodal d -wave gap function I.

The case I, whose nodes are on both the Fermi surfaces, is displayed in Fig. 7, while the case II (III), whose nodes are only on the inner (outer) Fermi surface.

As shown in Fig. 8, the asymmetric behavior with respect to the a -axis ($\phi = 0^\circ$) direction is found in the case of the nodal gap function II. Paying attention on the curve near $\phi = 0^\circ$ as shown in Fig. 9, the kink like structures are observed at around $\phi = \pm 15^\circ$ in an anti-symmetric manner. This calculation using the nodal gap function II is mostly consistent with the experimental results.¹⁸ These results suggest that the superconducting gap nodes lie on the inner Fermi surface in the 0-th band.

VI. DISCUSSION

First, we mention the electronic structure including the Fermi surfaces. In order to compare the present one with the previous tight-binding models^{21,40}, we construct the tight-binding model based on our band calculation taking account of the anion ordering. As shown in Fig. 10, the obtained tight-binding model is equivalent with that by the band calculation. Following the Ref. 21 in terms of the notation for the transfer integrals, the values we obtain are $t_{S1A} = 280$ meV, $t_{S2A} = 247$ meV, $t_{S1B} = 269$ meV, $t_{S2B} = 248$ meV, $t_{I1} = -47.0$ meV, $t_{I2} = -57.9$ meV, $t_{I3} = 48.0$ meV, $t_{I4} = -10.2$ meV, $t_{I5} = 63.3$ meV, and $t_{I6} = 3.98$ meV. These values are much more close to the values obtained by the band calculation without the anion ordering⁴⁰ than those obtained by phenomenologically taking account of the anion ordering.²¹ Therefore, the Fermi surfaces shown in Fig. 3 are found to be qualitatively different from those obtained by the previous tight-binding model considering the anion ordering.

Next, we discuss the assumption used in the gap examination, i.e., the excitation structure around vortex core is isotropic. In the Q1D superconductors, the superconducting gap amplitude may spatially vary around a vortex. However, low-lying quasiparticle excitations around a vortex are usually less affected by the variation

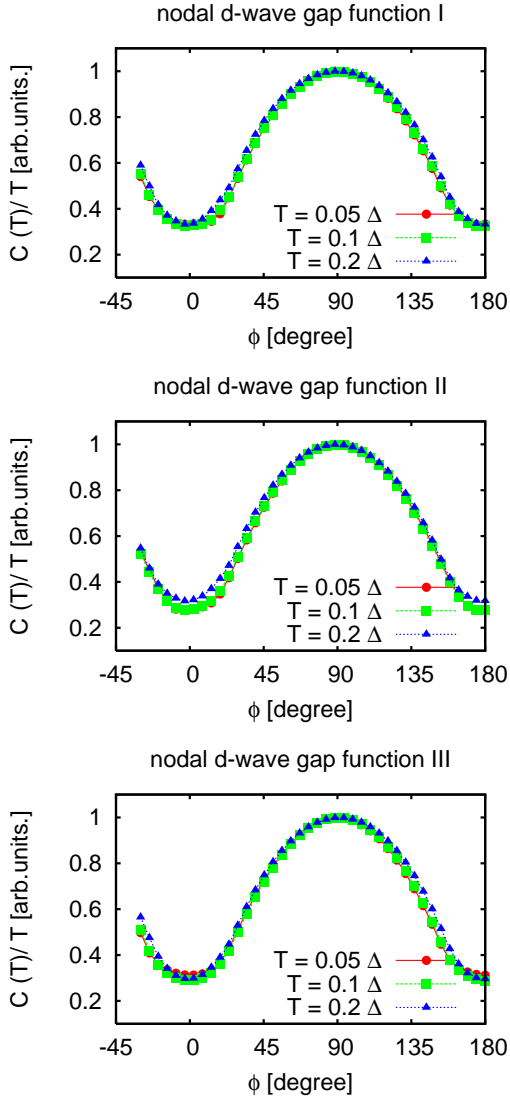


FIG. 8. (Color online) Angular dependence of the heat capacity rotating magnetic fields on a - b' plane in the case of the nodal d -wave gap function I, II, and III.

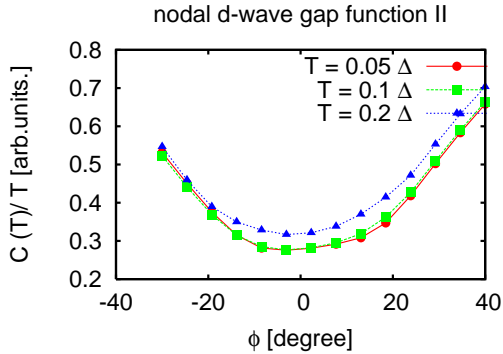


FIG. 9. (Color online) Angular dependence of the heat capacity rotating magnetic fields on a - b' plane in the case of the nodal d -wave gap function II.

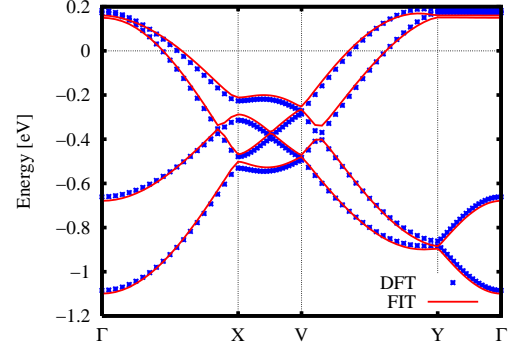


FIG. 10. (Color online) tight-binding fitted band structure (solid curves). the squares denote the first-principle band structure shown in Fig. 2.

of the gap amplitude than that of the superconducting phase.^{32,41} Our expression on the heat capacity shown in Eq. (38) can contain an anisotropic vortex core through $f(s, y)$. Therefore, it is a next-step checkpoint for the experimental consistency to investigate effects of the vortex core including the anisotropy.

Finally, we discuss the origin of the asymmetric behavior in the curves of the angle-resolved heat capacity. We calculate the partial heat capacity from each Fermi surface in the case of the nodal d -wave gap function I. As shown in Fig. 11, the kink structures of the angle-dependent partial heat capacity are different on each Fermi surface at $T = 0.05\Delta$. This difference originates from that in the Fermi velocity of the nodal quasiparticles on each Fermi surface. One finds that the asymmetric behaviors of the partial heat capacity are observed only in the case with the gap-nodes, since the distribution of the direction of the Fermi velocity does not have the strong asymmetry on the whole Fermi surfaces of $(\text{TMTSF})_2\text{ClO}_4$. Therefore, the asymmetric kink structure of the curves measured in the angle-resolved heat capacity is a clear evidence that the gap function has nodes in $(\text{TMTSF})_2\text{ClO}_4$.

VII. CONCLUSION

In order to examine the effects of the anion ordering and resolve the superconducting gap function in the organic superconductor $(\text{TMTSF})_2\text{ClO}_4$, we performed first-principles calculations and developed the quasi-classical theory, respectively. The first-principles calculation revealed that the anion ordering does not have any important role on the Fermi surface shapes in contrast that the gap opening around the crossing point was previously expected as a consequence of the ordering. The present calculation partly excludes the previous modeling based on the intuitive expectation. On the other hand, using Kramer-Pesch approximation on the single vortex core excitation together with the Fermi sur-

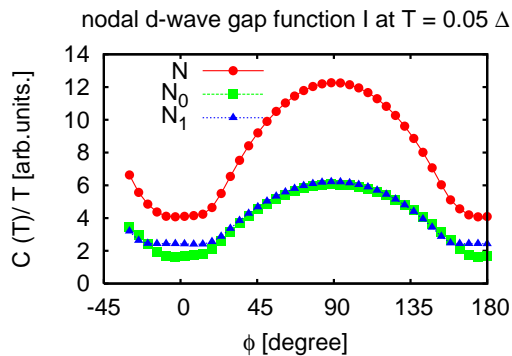


FIG. 11. (Color online) Angular dependence of the partial heat capacity rotating magnetic fields on a - b' plane in the case of the nodal d -wave gap function I at $T = 0.05\Delta$. N_i is the partial heat capacity on the i -th band.

faces obtained by the first-principles calculations, we constructed the formula calculating the angle-resolved heat capacity in the low-field range and compare the angle dependence obtained from various gap function models with the experimental results. Consequently, we showed that the nodal d -wave gap function consistently explains the experimental results. Especially, it should be emphasized that only the nodal d -wave gap function can reproduce the axis asymmetry of the angle dependence.

ACKNOWLEDGMENT

We thank N. Nakai, Y. Ota, and R. Igarashi for helpful discussions. We also thank S. Yonezawa for showing the latest experimental data.

- ¹ I. J. Lee, S. E. Brown, W. G. Clark, M. J. Strouse, M. J. Naughton, W. Kang, and P. M. Chaikin, *Phys. Rev. Lett.* **88**, 017004 (2002).
- ² J. Shinagawa, Y. Kurosaki, F. Zhang, C. Parker, S. E. Brown, D. Jérôme, J. B. Christensen, and K. Bechgaard, *Phys. Rev. Lett.* **98**, 147002 (2007).
- ³ K. Kuroki, *J. Phys. Soc. Jpn.*, **75**, 051013 (2006). and references therein.
- ⁴ H. Aizawa, K. Kuroki, Y. Tanaka, *J. Phys. Soc. Jpn.* **78**, 124711 (2009).
- ⁵ Y. Tanaka, and K. Kuroki, *Phys. Rev. B* **70**, 060502 (2004).
- ⁶ A. V. Rozhkov, *Phys. Rev. B* **79**, 224501 (2009).
- ⁷ N. Belmechri, G. Abramovici, and M. Héritier, *Europhys. Lett.* **82**, 47009 (2008).
- ⁸ H. Shimahara, *Phys. Rev. B* **61**, R14936 (2000).
- ⁹ K. Kuroki, R. Arita, and H. Aoki, *Phys. Rev. B* **63**, 094509 (2001).
- ¹⁰ N. Joo, P. Auban-Senzier, C. R. Pasquier, D. Jérôme
- ¹¹ M. Takigawa, H. Yasuoka, G. Saito, *J. Phys. Soc. Jpn.* **56**, 873 (1987).
- ¹² S. Belin and K. Behnia, *Phys. Rev. Lett.* **79**, 2125 (1997).
- ¹³ T. Sakakibara, A. Yamada, J. Custers, K. Yano, T. Tayama, H. Aoki, and K. Machida, *J. Phys. Soc. Jpn.* **76**, 051004 (2007).
- ¹⁴ Y. Matsuda, K. Izawa, I. Vekhter, *J. Phys. Condens. Matter* **18**, R705 (2006).
- ¹⁵ Y. Nagai and N. Hayashi, *Phys. Rev. Lett.* **101**, 097001 (2008).
- ¹⁶ Y. Nagai, Y. Kato, N. Hayashi, K. Yamauchi and H. Harima, *Phys. Rev. B* **76**, 214514 (2007).
- ¹⁷ Y. Nagai, N. Hayashi, Y. Kato, K. Yamauchi, and H. Harima, *J. Phys. Conf. Ser.* **150**, 052177 (2009).
- ¹⁸ S. Yonezawa, Y. Maeno, and K. Bechgaard, International Conference on Science and Technology of Synthetic Metals 2010 (ICSM2010) 6Ax-09 (unpublished).
- ¹⁹ J.-P. Pouget, G. Shirane, K. Bechgaard, J. M. Fabre, *Phys. Rev. B* **27**, 5203 (1985).
- ²⁰ P. C. W. Leung, A. J. Schultz, H. H. Wang, T. J. Emge, G. A. Ball, D. D. Cox, and J. M. Williams, *Phys. Rev. B* **30**, 1615 (1984).
- ²¹ D. Le Pévelen, J. Gaultier, Y. Barrans, D. Chasseau, F. Castet, and L. Duccase, *Eur. Phys. J. B* **19**, 363 (2001).
- ²² N. Kopnin, *Theory of Nonequilibrium Superconductivity* (Clarendon, Oxford, 2001).
- ²³ G. Eilenberger, *Z. Phys.* **214**, 195 (1968).
- ²⁴ A. Larkin and Yu. Ovchinnikov, *Zh. Eksp. Teor. Fiz.* **55**, 2262 (1968) [*Sov. Phys. JETP* **34**, 668 (1969)].
- ²⁵ Y. Kato, *J. Phys. Soc. Jpn.* **69**, 3378 (2000).
- ²⁶ Y. Nagato, K. Nagai and J. Hara, *J. Low Temp. Phys.* **93**, 33 (1993).
- ²⁷ S. Higashitani and K. Nagai, *J. Phys. Soc. Jpn.* **64**, 549 (1995).
- ²⁸ Y. Nagato, S. Higashitani, K. Yamada and K. Nagai, *J. Low Temp. Phys.* **103**, 1 (1996).
- ²⁹ N. Schopohl and K. Maki, *Phys. Rev. B* **52**, 490 (1995).
- ³⁰ N. Schopohl, arXiv:cond-mat/9804064 (unpublished).
- ³¹ Y. Nagai, Y. Kato, and N. Hayashi, *J. Phys. Soc. Jpn.* **75**, 043706 (2006).
- ³² Y. Nagai, Y. Ueno, Y. Kato and N. Hayashi, *J. Phys. Soc. Jpn.* **75**, 104701 (2006).
- ³³ A. S. Mel'nikov, D. A. Ryzhov, and M. A. Silaev, *Phys. Rev. B* **78**, 064513 (2008).
- ³⁴ T. Dahm, S. Graser, C. Iniotakis, and N. Schopohl, *Phys. Rev. B* **66**, 144515 (2002).
- ³⁵ G. Kresse and J. Hafner: *Phys. Rev. B* **47** (1993) RC558; G. Kresse and J. Furthmüller: *Phys. Rev. B* **54** (1996) 11169.
- ³⁶ J. P. Perdew, K. Burke, M. Ernzerhof: *Phys. Rev. Lett.* **77** (1996) 3865.
- ³⁷ P. E. Blöchl: *Phys. Rev. B* **50** (1994) 17953; G. Kresse and D. Joubert: *Phys. Rev. B* **59** (1999) 1758.
- ³⁸ B. Gallois, Ph.D thesis.
- ³⁹ W. Wu, I. J. Lee, and P. M. Chaikin, *Phys. Rev. Lett.* **91**, 056601 (2003).
- ⁴⁰ S. Ishibashi, A. A. Manuel, and M. Kohyama, *J. Phys. Condens. Matter* **11** 2279 (1999).
- ⁴¹ N. Hayashi, M. Ichioka, and K. Machida, *Phys. Rev. B* **56**, 9052 (1997).